



Noble metal free, CeO₂/LaMnO₃ hybrid achieving efficient photo-thermal catalytic decomposition of volatile organic compounds under IR light

Juan-Juan Li^{a,b}, En-Qi Yu^{a,b,c}, Song-Cai Cai^{a,b,c}, Xi Chen^{a,b,c}, Jing Chen^{c,d}, Hong-Peng Jia^{a,b,c,*}, Yi-Jun Xu^{e,f,**}

^a CAS Center for Excellence in Regional Atmospheric Environment, Institute of Urban Environment, Chinese Academy of Sciences, Xiamen 361021, PR China

^b Key Laboratory of Urban Pollutant Conversion, Institute of Urban Environment, Chinese Academy of Sciences, Xiamen 361021, PR China

^c University of Chinese Academy of Sciences, Beijing, 100049, PR China

^d Xiamen Institute of Rare-earth Materials, Haixi Institutes, Chinese Academy of Sciences, Xiamen, Fujian 361021, PR China

^e State Key Laboratory of Photocatalysis on Energy and Environment, College of Chemistry, New Campus, Fuzhou University, Fuzhou 350116, PR China

^f College of Chemistry, New Campus, Fuzhou University, Fuzhou 350116, PR China

ARTICLE INFO

Keywords:

CeO₂/LaMnO₃

IR light

Photo-thermocatalysis

VOCs

Mars-van Krevelen

ABSTRACT

Large amounts of anthropogenic VOCs emissions give rise to photochemical smog and ground-level ozone. Currently, catalytic oxidation for VOCs elimination still requires energy-intensive high temperatures. Light-driven photo-thermocatalysis oxidation of VOCs holds great promise to substantially reduce energy consumption for sustainable development in comparison with conventional thermal-based catalytic oxidation. Herein, CeO₂/LaMnO₃ composite, featuring the broad light wavelength absorption (800–1800 nm), can be used as a highly active photo-thermal responsive catalyst on VOCs decomposition under IR irradiation. The maximum photo-thermal conversion efficiency is able to reach 15.2% with a significant toluene conversion of 89% and CO₂ yield of 87% under IR irradiation intensity of 280 mW/cm², together with excellent stability of nearly 30 h. Comparative characterizations reveal that such photo-thermal catalytic activity enhancement is predominantly attributed to the synergistic effects of ultrabroadband strong light absorption, efficient light-to-heat conversion, good low temperature reducibility and high lattice oxygen mobility, originating from an intense interaction of LaMnO₃ with CeO₂. Toluene oxidation reaction on CeO₂/LaMnO₃ catalyst proceeds via a Mars-van Krevelen mechanism as evidenced by *in situ* diffuse reflectance infrared Fourier transform spectroscopy.

1. Introduction

Volatile organic compounds (VOCs), generated from numerous anthropogenic activities (*i.e.* vehicular and industrial emissions from fossil fuel combustion) and additional natural sources (*i.e.* biogenic terrestrial ecosystems, biomass burning and plant decay) [1], are increasingly emitted into the atmosphere. A variety of aromatic VOCs with high toxicity or carcinogenic, mutagenic and teratogenic features, are harmful to human health and behave as the precursor of photochemical smog, tropospheric ozone and secondary aerosols, ultimately making major contributors to air pollution [2]. Consequently, numerous researchers have invested continuously growing interest for VOCs elimination by either physical deposition (*e.g.*, absorption, condensation and membrane separation) or catalytic oxidation to CO₂ (*e.g.*, thermal

catalytic oxidation, photocatalysis and plasma catalysis). In particular, catalytic oxidation is generally considered as the most efficient way to entirely decompose the wide range of organic pollutants into harmless products (CO₂ and H₂O). Supported noble metals, single or mixed transition metal oxides have been developed for the oxidation of VOCs. Notably, noble metal catalysts show prominent catalytic activity, but tend to have high cost, low thermal stability, easy sintering and poisoning characters.

Perovskite oxides, an important class of mixed oxide, have received significant attention, because they offer potential advantages in high catalytic activity, low cost, strong thermal stability and perfect anti-poisoning ability [3]. Previously, lanthanum manganese-based perovskites have been found to exhibit excellent catalytic performance for VOCs oxidation compared to other transition metal-based perovskites

* Corresponding author at: CAS Center for Excellence in Regional Atmospheric Environment, Institute of Urban Environment, Chinese Academy of Sciences, Xiamen 361021, PR China.

** Corresponding author at: State Key Laboratory of Photocatalysis on Energy and Environment, College of Chemistry, New Campus, Fuzhou University, Fuzhou 350116, PR China.

E-mail addresses: hpjia@iue.ac.cn (H.-P. Jia), yjxu@fzu.edu.cn (Y.-J. Xu).

<https://doi.org/10.1016/j.apcatb.2018.08.069>

Received 12 June 2018; Received in revised form 1 August 2018; Accepted 28 August 2018

Available online 29 August 2018

0926-3373/ © 2018 Elsevier B.V. All rights reserved.

[4]. For example, Levasseur et al. [5] prepared a series of LaBO_3 ($B = \text{Co, Mn, and Fe}$) catalysts by adopting reactive grinding approach and observed their different activities for methanol oxidation following the sequence $\text{LaMnO}_3 > \text{LaCoO}_3 > \text{LaFeO}_3$, which was ascribed to easy reducibility and high availability of surface oxygen of LaMnO_3 . Álvarez-Galván and co-workers [6] studied catalytic combustion of methyl ethyl ketone over LaBO_3 ($B = \text{Cr, Co, Ni and Mn}$), and the order of catalytic activity is $\text{LaMnO}_3 > \text{LaCoO}_3 \approx \text{LaNiO}_3 > \text{LaCrO}_3$, being comparable with that of more expensive supported Pt catalysts. In addition, $\text{Al}_2\text{O}_3/\text{LaMnO}_3$, $\text{TiO}_2/\text{LaMnO}_3$ and $\text{CeO}_2/\text{LaMnO}_3$ have also been reported for thermal-based catalytic oxidation of VOCs [7].

In contrast to thermal catalytic oxidation of VOCs as mentioned above, solar energy represents a non-polluting, renewable and economical energy source [8]. Converting solar light into chemical energy via photocatalysis to generate highly reactive oxidative species (ROs, e.g., holes or superoxide/hydroxyl radicals) can be used as an effective strategy for photocatalytic degradation of VOCs [9–11]. The long wavelength infrared (IR) light constitutes 53% of the solar energy reaching earth's surface [12], and it is highly desirable to develop IR-light-response photocatalysts for degradation of VOCs. Recently, we found that the hybrid Pt-rGO- TiO_2 [13], featuring the broad light wavelength absorption, can be used as a highly active photo-thermal responsive catalyst for efficient VOCs decomposition under IR irradiation, which suggests that IR-driven photo-thermocatalysis opens the alternative possibility of light-driven photo-thermal catalytic oxidation for environmental pollutants elimination.

In general, the wide light absorption capability covering the IR spectrum range, forceful coupling of the harvested photons into thermal energy and highly efficient thermocatalytic activity are fundamental prerequisites for an ideal photo-thermal material to achieve high solar energy conversion efficiency. It has been shown that LaMnO_3 perovskite is characteristic of well-defined IR-absorption capability, deriving from free Jahn-Teller hole polarons and Jahn-Teller hole polarons within localized charge transfer vibronic excitons (Mn^{4+} - Mn^{2+} pairs) [14–16]. Up to now, the main focus of interests in LaMnO_3 -based composites have been on thermocatalysis and UV-vis light driven photocatalysis, rather than IR-light driven catalysis. For example, Li and co-workers [17] have investigated lanthanum-based perovskites LaBO_3 ($B = \text{Cr, Mn, Fe, Co and Ni}$) for photo-thermocatalytic oxidation of gaseous styrene under visible light illumination and found that styrene oxidation activities follow the order of $\text{LaMnO}_3 > \text{LaFeO}_3 > \text{LaNiO}_3 > \text{LaCoO}_3 > \text{LaCrO}_3$. However, to date, there has been no report on utilizing a LaMnO_3 -based material for IR-driven photo-thermal catalytic reactions.

Herein, we report that the non-noble metal $\text{CeO}_2/\text{LaMnO}_3$ nano-material as a novel IR light absorber for efficient degradation of VOCs through photo-thermal effect. In particular, the $\text{CeO}_2/\text{LaMnO}_3$ composite exhibits high catalytic performance with 89% of toluene conversion and 87% of CO_2 yield under IR irradiation intensity of 280 mW/cm^2 , along with excellent stability of nearly 30 h. The comparative characterizations reveal that such photo-thermal catalytic activity enhancement benefits from the synergistic effects of strong light absorption, efficient light-to-heat conversion, increased low temperature reducibility and accelerated lattice oxygen mobility. Our current work strongly suggests that there is also a wide promising scope to explore the IR light driven LaMnO_3 -based composites in heterogeneous photo-thermal catalysis. It is anticipated that this work would enable the extensive development of photo-thermal responsive perovskites for solar energy conversion.

2. Experimental section

2.1. Catalyst preparation

$\text{CeO}_2/\text{LaMnO}_3$ was synthesized via citric acid combustion method. First, stoichiometric amounts of $\text{La}(\text{NO}_3)_3 \cdot 6\text{H}_2\text{O}$, $\text{Mn}(\text{NO}_3)_2$ (50 wt%

aqueous solution) and $\text{Ce}(\text{NO}_3)_3 \cdot 6\text{H}_2\text{O}$ were dissolved in 200 ml of deionized water. Then, citric acid was added into the above solution with a molar ratio of 1:3 to the total amount of metal cations. Subsequently, the solution was heated under vigorous stirring on a hot plate until self-combustion occurred. Finally, $\text{CeO}_2/\text{LaMnO}_3$ catalysts were obtained by calcination at 400°C for 2 h and then at 800°C for 4 h.

For comparison, the preparation procedure of LaMnO_3 and CeO_2 were similar to that of $\text{CeO}_2/\text{LaMnO}_3$ without addition of CeO_2 or LaMnO_3 precursor, respectively.

2.2. Catalyst characterization

Powder X-ray diffraction (XRD) characterization was carried out on a X'Pert Pro automatic powder diffractometer operated at 40 kV and 40 mA using $\text{Cu K}\alpha$ monochromatized radiation. Nitrogen adsorption-desorption measurements of the catalysts were performed on a Quantachrome autosorb iQ2 adsorption automatic instrument at liquid nitrogen temperature. All samples were degassed under vacuum at 250°C for 10 h before the measurement. The specific surface area and pore volume of the catalysts were calculated from the nitrogen adsorption-desorption isotherms using the Brunauer-Emmett-Teller (BET) and Barrett-Joyner-Halenda (BJH) methods, respectively. The optical properties of the samples were characterized by UV-vis diffuse reflectance spectroscopy (DRS) using UV-vis spectrophotometer (UV 3600, Shimadzu) at room temperature using BaSO_4 as a reference. XPS analysis was conducted on a Thermo Escalab 250 with a monochromatized microfocused Al X-ray source. Scanning electron microscopy (SEM) images of the samples were obtained on an S-4800 scanning electron microscopy. Transmission electron microscopy (TEM) was analyzed using a JEOL model JEM 2100 EX instrument at an acceleration voltage of 200 kV. The enthalpy of the sample was obtained by using differential scanning calorimeter (Netzsch STA 449 F3, Thermal Analysis Corporation, Germany) from 30 to 400°C at a heating rate of 5°C/min in an air flow of 50 ml/min . O_2 -Temperature-programmed desorption (TPD) measurement was performed on a Quantachrome Chemstar instrument. 200 mg sample was filled in an adsorption vessel and pretreated in a He flow (50 ml/min) at 300°C for 60 min then cooled to 35°C and kept at this temperature for 60 min in a flow of 5 vol % O_2/He . Then, the sample was swept with He for 60 min and heated to 900°C at a rate of 10°C/min in a He flow of 30 ml/min . The desorbed oxygen was monitored by thermal conductivity detector. *In situ* DRIFTS was performed on a FTIR spectrometer (Thermo Fisher Nicolet iS50) equipped with a smart collector and a MCT/A detector.

2.3. Photo-thermocatalytic activity

The photo-thermocatalytic activity of the samples for toluene oxidation was evaluated in a cylindrical stainless steel reactor with a quartz window under IR light irradiation (375 W, Philips) with a 800 nm cut-off filter. In the experiments, an ethanol suspension containing 0.1 g of the catalyst was prepared, and then coated on a fibreglass membrane of 50 mm diameter, dried at 80°C and finally placed on the photoreactor. Prior to irradiation, the adsorption-desorption equilibrium of toluene on the photocatalyst was conducted. The simulated air stream (21% O_2/N_2) containing 200 ppm of toluene passed through the catalyst layer (0.1 g) with the total flow rate of 52.2 mL/min , giving a gas hourly space velocity (GHSV) of $31,320 \text{ mL/(g h)}$. The concentration of toluene and the evolution of CO_2 were monitored by an on-line gas chromatograph equipped with two flame ionization detectors (FID) and a nickel-based methanizer. The toluene conversion, CO_2 yield, toluene degradation rate and CO_2 production rate for the photocatalytic reaction were calculated by using Eqs. (1)–(4), respectively.

$$\text{Toluene conversion (\%)} = 100\% \times ([\text{Toluene}]_{\text{in}} - [\text{Toluene}]_{\text{out}})/[\text{Toluene}]_{\text{in}} \quad (1)$$

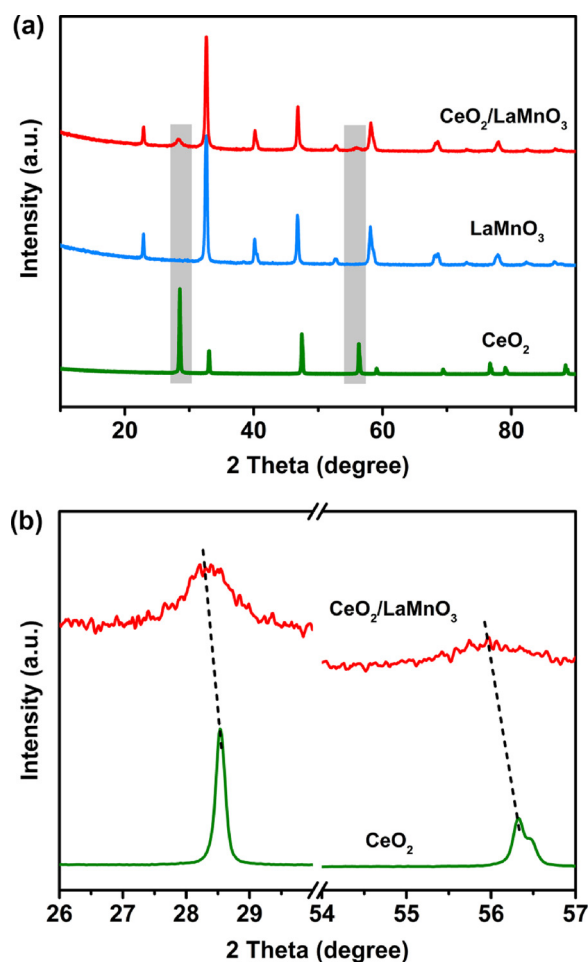


Fig. 1. (a) XRD patterns of $\text{CeO}_2/\text{LaMnO}_3$, LaMnO_3 and CeO_2 catalysts; (b) magnified peaks of 2θ at around 28.2° and 56.0° .

$$\text{CO}_2 \text{ yield (\%)} = 100\% \times [\text{CO}_2]_{\text{produced}} / [\text{CO}_2]_{\text{theoretical}} \quad (2)$$

$$\text{Toluene degradation rate } (\mu\text{mol g}^{-1} \text{ min}^{-1}) = ([\text{Toluene}]_{\text{in}} - [\text{Toluene}]_{\text{out}}) / (\text{mass time}) \quad (3)$$

$$\text{CO}_2 \text{ production rate } (\mu\text{mol g}^{-1} \text{ min}^{-1}) = [\text{CO}_2]_{\text{produced}} / (\text{mass time}) \quad (4)$$

3. Results and discussion

The XRD patterns of the $\text{CeO}_2/\text{LaMnO}_3$ composite, along with LaMnO_3 and CeO_2 references are shown in Fig. 1(a). It is obvious that the $\text{CeO}_2/\text{LaMnO}_3$ sample exhibits diffraction peaks corresponding to cubic LaMnO_3 perovskite phase and cubic CeO_2 crystalline phase, where the peaks at 2θ value of 22.9° , 32.7° , 40.2° , 46.9° , 52.8° , 58.2° , 68.1° , 73.1° , 78.0° , 82.4° and 86.8° are indexed to (100), (110), (111), (200), (210), (211), (220), (300), (310), (311) and (222) crystal planes of LaMnO_3 (JCPDS PDF # 01-075-0440) and the peaks at 2θ value of 28.2° and 56.0° are assigned to (111) and (311) crystal planes of CeO_2 (JCPDS PDF # 01-089-8436), respectively. It can be seen from the enlarged scale of 2θ at around 28.2° and 56.0° in Fig. 1(b) that the peaks corresponding to CeO_2 in $\text{CeO}_2/\text{LaMnO}_3$ sample slightly shift to lower diffraction angles compared with that of pure CeO_2 (JCPDS PDF # 01-081-0792) sample, indicating an intense interaction between LaMnO_3 and CeO_2 .

The microscopic structure of $\text{CeO}_2/\text{LaMnO}_3$ composite was characterized by SEM. As can be seen in Fig. 2(a) and (b), the surface morphologies of LaMnO_3 -based perovskites are similar, both of which

are composed of irregularly morphological interconnected sub-microparticles with a length of $0.1\text{--}0.5\text{ }\mu\text{m}$, revealing a porous structure with interconnected nano-sized particles. Fig. 2(c) presents the agglomeration of CeO_2 NPs in the uniform size distribution with the average size of $40\text{--}50\text{ nm}$. Moreover, TEM and HRTEM are further performed to look into the detailed morphology of $\text{CeO}_2/\text{LaMnO}_3$. As can be seen in Fig. 2(d) and (e), these interconnected nanoparticles are highly crystalline and the fast Fourier transform (FFT) patterns of the selected areas marked by the red and blue frame authenticate LaMnO_3 cubic perovskite nanocrystals with 0.274 nm lattice spacing of (110) facet and CeO_2 cubic nanocrystals with 0.314 nm lattice spacing of (111) facet, respectively. A selected area electron diffraction (SAED) was carried out to record bright electron diffraction rings aiming at identifying the crystal structure of $\text{CeO}_2/\text{LaMnO}_3$ composite. The inset in Fig. 2(e) indicates the formation of polycrystalline structure, which coincides with the XRD result. Furthermore, the elemental distributions in the $\text{CeO}_2/\text{LaMnO}_3$ composite were mapped by the energy dispersive X-ray (EDX) spectroscopic technique. As shown in Fig. 2(f), the elements of La, Mn, Ce and O distributed uniformly within the $\text{CeO}_2/\text{LaMnO}_3$ composite, suggesting that the CeO_2 is homogeneous introduced into the LaMnO_3 .

UV–vis diffuse reflectance spectra (DRS) measurement was performed to evaluate the optical response of the catalysts. Fig. 3 shows the absorption spectra of $\text{CeO}_2/\text{LaMnO}_3$ composite as compared with those of pure CeO_2 and LaMnO_3 catalysts. The pure CeO_2 looks pale yellow (inset in Fig. 3) and displays two typical absorption edges (305 and 398 nm) with intense transition in the UV region, as a result of the charge-transfer transition from O 2p to Ce 4f/Ce 5d orbitals in the intrinsic band gap absorption of CeO_2 [18,19], but with almost no absorption in the Vis-IR region. The bare LaMnO_3 with a color of black exhibits a strong absorption of 95.1% over the whole range of $300\text{--}1800\text{ nm}$ with an obvious red shift at the absorption, arising from the polaron-like states within localized charge transfer vibronic excitons [15,16]. For the $\text{CeO}_2/\text{LaMnO}_3$ composite, its color still shows black and the absorption coefficient is further enhanced to 95.5% over Vis-IR light region, suggesting that the introduction of CeO_2 into LaMnO_3 is able to effectively promote the Vis-IR response, which can be attributed to electronic interactions between CeO_2 and LaMnO_3 [20] as well as reduced reflection of light [21]. An ideal light absorber that a dark material absorbs radiation at all angles and polarizations [22], which demonstrates its possible potential as a suitable catalyst that efficiently absorbs light and releases the absorbed photons in the form of heat (photo-thermal effect), resulting in a considerable increase of temperature, enough to trigger/accelerate catalytic reactions. The LaMnO_3 -based catalysts, featuring the broad light wavelength absorption ($800\text{--}1800\text{ nm}$), can thus be expected to be a highly active photo-thermal responsive catalyst toward a target reaction through creating a pronounced temperature increase under IR irradiation.

To confirm whether the broad IR absorption identified for LaMnO_3 -based material is capable of driving solar energy conversion, the catalytic activity of $\text{CeO}_2/\text{LaMnO}_3$ composite was evaluated by catalytic oxidation of gaseous toluene under IR light irradiation. The catalytic performance of $\text{CeO}_2/\text{LaMnO}_3$ composite under IR lamp with different light intensities as a function of irradiation time is illustrated in Fig. 4(a) and (b). As expected, $\text{CeO}_2/\text{LaMnO}_3$ composite shows much higher catalytic activity than CeO_2 and LaMnO_3 monocomponent under identical irradiation intensity. Remarkably, the conversion of toluene and yield of CO_2 greatly increase with elevated light intensities from 156 , 190 , 240 to 280 mW/cm^2 . Specifically, the catalytic activities of these samples follow the sequence $\text{CeO}_2/\text{LaMnO}_3 > \text{LaMnO}_3 > \text{CeO}_2$. Within 120 min of IR irradiation of 280 mW/cm^2 , the $\text{CeO}_2/\text{LaMnO}_3$ composite shows the most active for catalytic oxidation of toluene with the maximum toluene conversion of 89% and CO_2 yield of 87%. As reflected by Fig. 4(c) and (d), the degradation efficiency over $\text{CeO}_2/\text{LaMnO}_3$ composite is provided with toluene degradation rate of $0.198\text{ }\mu\text{mol g}^{-1} \text{ min}^{-1}$ and CO_2 production rate of $7.090\text{ }\mu\text{mol}$

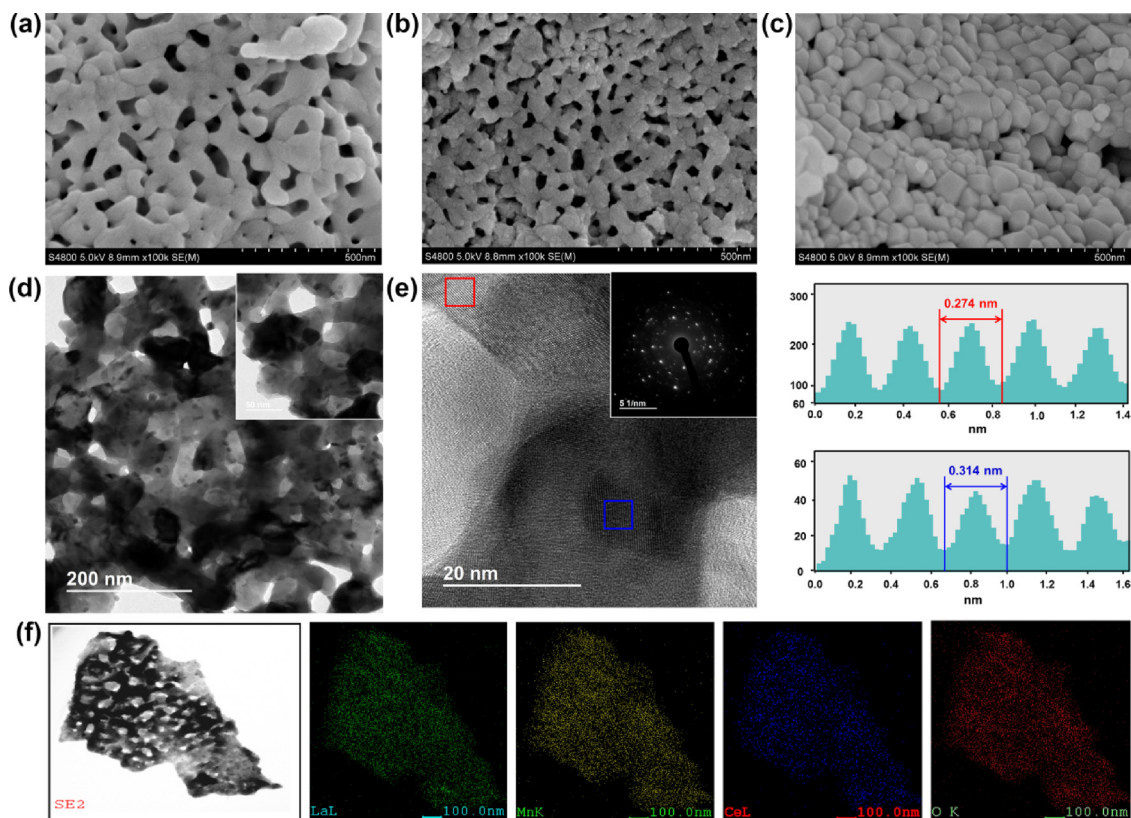


Fig. 2. SEM and TEM images of (a) LaMnO_3 , (b, d) $\text{CeO}_2/\text{LaMnO}_3$ and (c) CeO_2 (inset in (d) shows the high magnification TEM image); (e) The high-resolution TEM (HRTEM) images of the selected area in panel d (note that inset is a selected area electron diffraction (SAED) pattern and the right images of panels e are the fast Fourier transform (FFT) pattern of the area marked by the red and blue square box and the corresponding intensity profiles, respectively); and (f) TEM-EDX elemental mapping of La, Mn, Ce and O distribution of $\text{CeO}_2/\text{LaMnO}_3$ composite. (For interpretation of the references to colour in this figure legend, the reader is referred to the web version of this article).

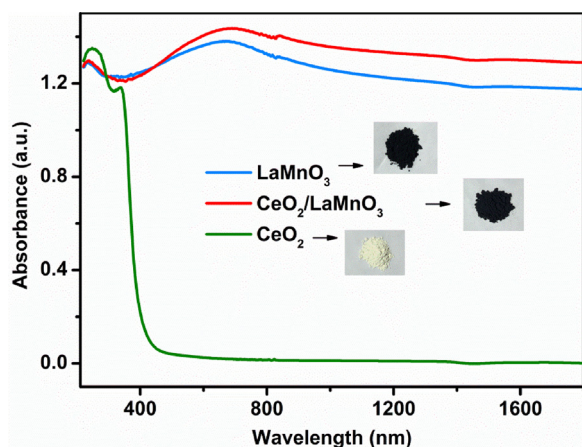


Fig. 3. UV-vis DRS of $\text{CeO}_2/\text{LaMnO}_3$, LaMnO_3 and CeO_2 catalysts (For interpretation of the references to colour in the figure text, the reader is referred to the web version of this article).

$\text{g}^{-1} \text{min}^{-1}$, which is much higher than that of 0.002 and $0 \mu\text{mol g}^{-1} \text{min}^{-1}$ over CeO_2 and that of 0.016 and $1.076 \mu\text{mol g}^{-1} \text{min}^{-1}$ over LaMnO_3 , respectively. It is noted that the degradation efficiency depends on the light intensity where the degradation efficiency increases remarkably as the light intensity increases. These results demonstrate that the homogeneous introduction of CeO_2 into LaMnO_3 induces significant improvement in the IR-driven photodegradation efficiency. The TOF of the catalysts were estimated on the assumption that all the Mn^{4+} were accessible to the reactants. Fig. S2 shows the dependence of TOF_{Mn} on the reaction temperature in the photo-thermal catalytic

decomposition of toluene at a conversion less than 20% over $\text{CeO}_2/\text{LaMnO}_3$ and LaMnO_3 catalysts. The TOF_{Mn} over each catalyst increases as the reaction temperature increases. The TOF of $\text{CeO}_2/\text{LaMnO}_3$ is 0.120 s^{-1} at 198°C and dramatically increases to 0.191 s^{-1} at 218°C . In contrast, the TOFs of LaMnO_3 are 0.022 s^{-1} at 198°C and 0.083 s^{-1} at 218°C , respectively. The result confirms that the catalytic activity of $\text{CeO}_2/\text{LaMnO}_3$ is intrinsically superior to that of LaMnO_3 . To gain further insight into the synergy effect between CeO_2 and LaMnO_3 , apparent activation energies (E_{app}) of CO_2 yield below 20% mineralization of toluene is calculated according to the slope values for linear-fitting Arrhenius plots in Fig. 4(e) [25,26]. The result reveals that the E_{a} values decrease in the following order: CeO_2 (105.98 kJ/mol) > LaMnO_3 (101.77 kJ/mol) > $\text{CeO}_2/\text{LaMnO}_3$ (83.98 kJ/mol). Obviously, $\text{CeO}_2/\text{LaMnO}_3$ composite displays much lower activation energy than pure CeO_2 and LaMnO_3 , indicating that toluene oxidation over $\text{CeO}_2/\text{LaMnO}_3$ catalyst proceeds much easier [27]. This result confirms that the homogeneous introduction of Ce into LaMnO_3 to form $\text{CeO}_2/\text{LaMnO}_3$ composite performs excellently in catalyzing the complete oxidation of toluene [28]. Impressively, the stability experiment of $\text{CeO}_2/\text{LaMnO}_3$ composite shown in Fig. 4(f) clearly exhibits that the toluene conversion and CO_2 yield are close to 76% and 60% over consecutive irradiation of 30 h (a cycle for 2 h, 15 cycles) under IR irradiation with 260 mW/cm^2 light intensity.

To further identify whether the high catalytic activity of $\text{CeO}_2/\text{LaMnO}_3$ under IR irradiation arises from photocatalysis, the photocatalytic activity of $\text{CeO}_2/\text{LaMnO}_3$ composite for toluene oxidation was performed. 100 mg of $\text{CeO}_2/\text{LaMnO}_3$ was coated on a cylindrical quartz reactor ($5 \text{ cm} \times 5 \text{ cm} \times 1 \text{ cm}$) and then the reactor was placed in a glycerol-water bath of ultralow temperature (-20°C) to ensure the photocatalytic reaction with IR irradiation of 280 mW/cm^2 has cooled

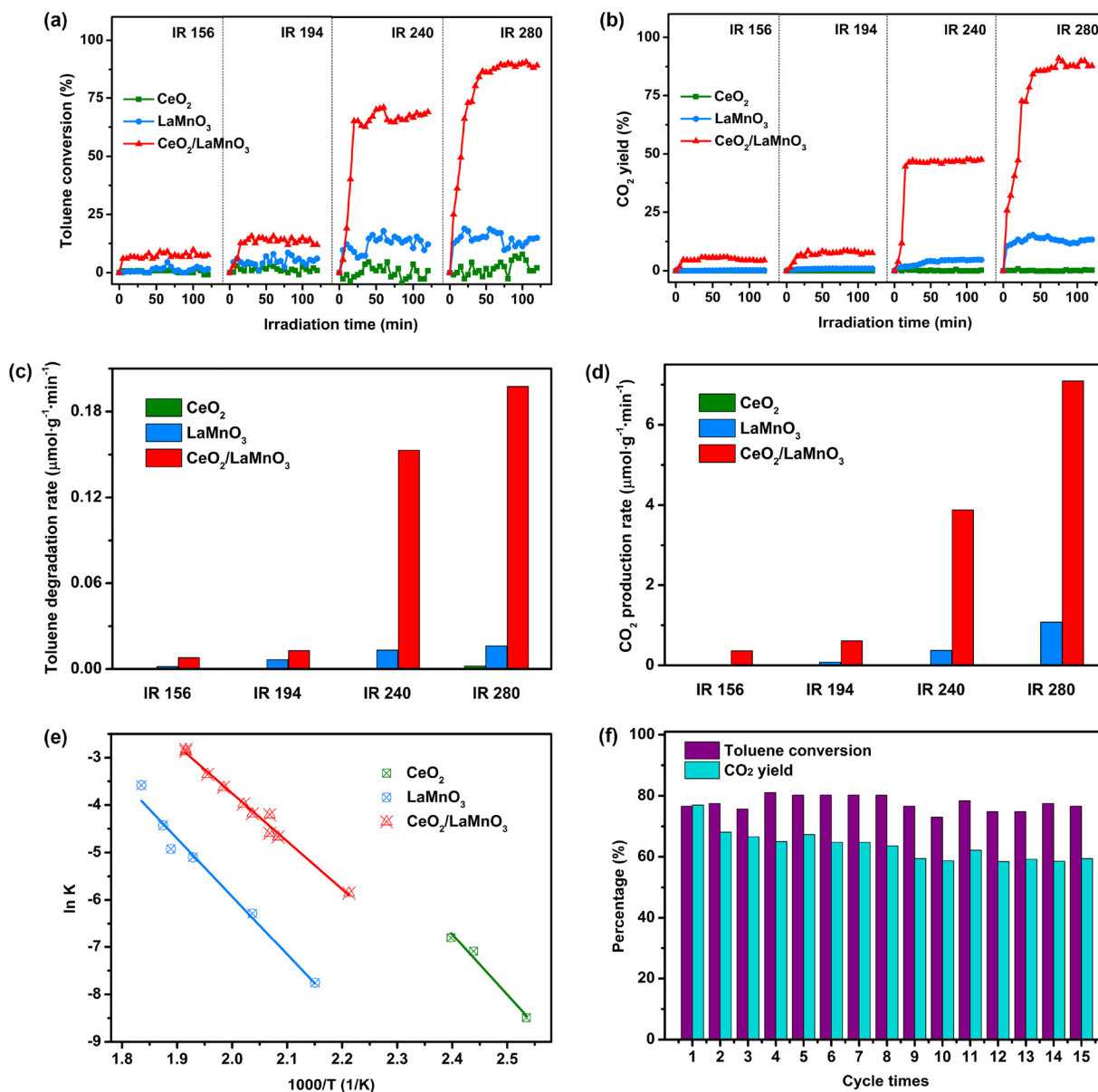


Fig. 4. (a) Time course of toluene conversion, (b) CO_2 yield, (c) toluene degradation rate and (d) CO_2 production rate at 120 min over CeO_2 , LaMnO_3 and $\text{CeO}_2/\text{LaMnO}_3$ under IR irradiation with various light intensities (156, 194, 240 and 280 mW/cm^2); (e) linear-fitting Arrhenius plots of $\text{CeO}_2/\text{LaMnO}_3$, LaMnO_3 and CeO_2 catalysts and (f) the durability of $\text{CeO}_2/\text{LaMnO}_3$ composite for toluene oxidation with IR irradiation of 260 mW/cm^2 under steady state conditions.

to a temperature below which light-off occurs. As shown in Fig. S3, neither distinct photo-degradation of toluene nor discernable generation of CO_2 can be clearly observed, indicating that the $\text{CeO}_2/\text{LaMnO}_3$ is IR light photocatalytically inert material toward the oxidation of toluene which is possibly attributed to (1) wide-bandgap of bulk CeO_2 (3.15 eV) [29], not being able to be activated by the inadequate excitation energy of IR photon, and (2) the narrow bandgap of LaMnO_3 endowed the holes in the composite with insufficient oxidation capacity and ineffective transfer to the VB of CeO_2 , resulting in a quick depletion of excitation energy. The experimental and theoretical studies of IR-absorption in previous research works [14–16] indicate that LaMnO_3 single crystal has led to the observation of well-defined IR-absorption peaks in connection with free Jahn-Teller hole polarons and Jahn-Teller hole polarons within localized charge transfer vibronic excitons ($\text{Mn}^{4+}-\text{Mn}^{2+}$ pairs), which may give LaMnO_3 and LaMnO_3 -based materials unique thermal properties, where LaMnO_3 as nanometer-sized heater can strongly absorb IR light and effectively convert it into thermal energy to raise the temperature of material.

As shown in Fig. 5(a), the temperatures of bare LaMnO_3 and $\text{CeO}_2/\text{LaMnO}_3$ composite quickly increase from room temperature to around 198 °C, 219 °C, 255 °C and 275 °C with the lamp on the light intensities of 156, 194, 240 and 280 mW/cm^2 , respectively. When the temperature reaches a plateau, an equilibrium is established between the absorption of light energy and the energy dissipation from the catalyst to the surroundings [30]. The plateau temperatures of the catalysts displayed in Fig. 5(b) demonstrate direct evidence for their efficient photo-thermal conversion, which was expected to trigger and accelerate chemical reactions nearby. Obviously, the positive relationship between toluene degradation rate/ CO_2 production rate and light intensity can be explained by a photo-thermal effect since a stronger light intensity results in a higher reaction temperature, which is extremely favorable for endothermic reactions, i.e., catalytic oxidation of toluene. Significantly, these observations indicate that the efficient infrared light promoted degradation of toluene over $\text{CeO}_2/\text{LaMnO}_3$ composite should be closely associated with the photo-thermocatalysis. The photo-thermal conversion efficiency (η) is defined as the ratio of the converted

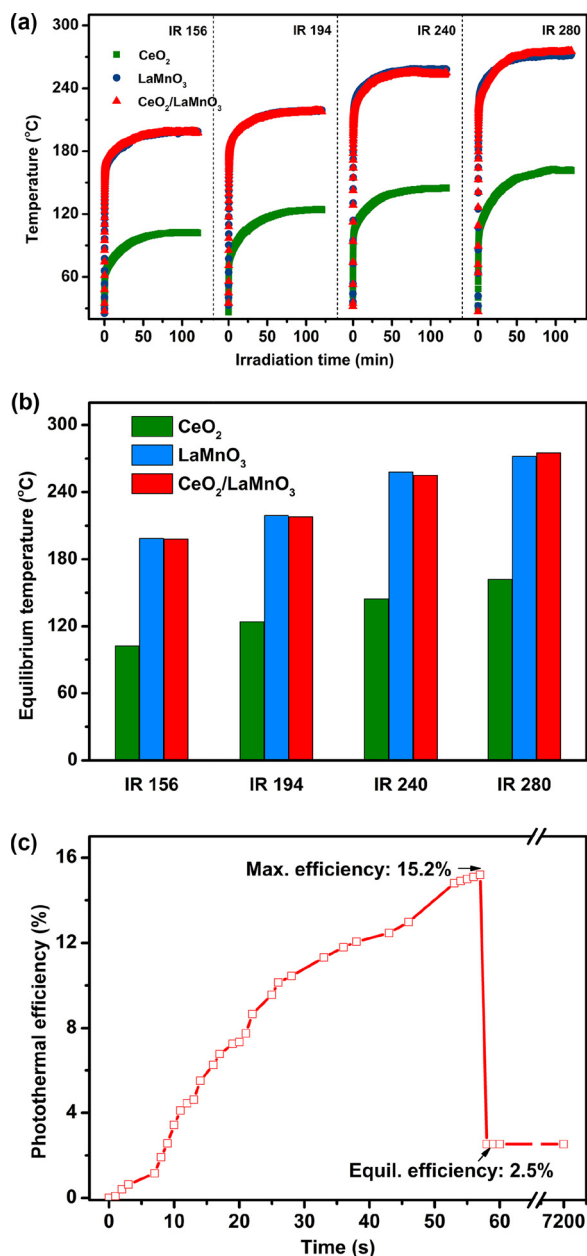


Fig. 5. (a) The temperature curve of CeO₂, LaMnO₃ and CeO₂/LaMnO₃ materials upon IR irradiation with various light intensities (156, 194, 240 and 280 mW/cm²), (b) the corresponding equilibrium temperature and (c) photothermal conversion efficiency of CeO₂/LaMnO₃ composite under IR irradiation of 280 mW/cm².

thermal energy to the incident light energy [31] where the maximum efficiency and equilibrium efficiency reach 15.2% and 2.5% for CeO₂/LaMnO₃ composite under IR irradiation of 280 mW/cm², respectively, which is shown in Fig. 5(c).

With the goal of understanding the origin of observed efficient infrared light promoted degradation of toluene over photo-thermal responsive CeO₂/LaMnO₃ composite, a series of characterizations such as BET, H₂-TPR, toluene-TPD, O₂-TPD and XPS were further carried out to explore the textural structures and physicochemical properties of the material. N₂ adsorption-desorption isotherms of the CeO₂/LaMnO₃, along with CeO₂ and LaMnO₃ samples are shown in Fig. S4 and their pore parameters/BET surface areas are summarized in Table 1. It is obvious that all of the samples display a similar type IV isotherm, showing pore condensation with remarkable adsorption-desorption

Table 1

Physical structural parameters, surface elemental compositions and quantitative results of H₂-TPR.

| Entry | CeO ₂ /LaMnO ₃ | LaMnO ₃ | CeO ₂ |
|--|---|--------------------|------------------|
| Absorbance (%) ^a | 95.5 | 95.1 | 0.0 |
| S _{BET} (m ² g ⁻¹) | 12.775 | 14.275 | 9.658 |
| Pore volume (cm ³ g ⁻¹) | 0.092 | 0.114 | 0.097 |
| E _a (kJ/mol) | 83.98 | 101.77 | 105.98 |
| TOF _{Mn} (s ⁻¹) | 198 °C 218 °C | 0.120 0.191 | 0.022 0.083 |
| Surface element molar ratio ^b | Mn ⁴⁺ /Mn ³⁺ O _{latt} /O _{ads} | 0.472 1.351 | 0.489 0.770 |
| H ₂ consumption ^c (μmol/g) | 50–910 °C ≥ 500 °C | 3373.9 2077.9 | 920.8 859.9 |

^a Absorbance ($a = \int (1 - R(\lambda)) \cdot E_{IR} / \int E_{IR}$ (800 ≤ λ ≤ 1800 nm) from Fig. S1 [23,24].

^b Surface elemental compositions from XPS.

^c H₂ consumption from H₂ TPR profiles.

hysteresis, which indicates that these samples are materials with mesoporous structures. The corresponding surface area and pore volume are calculated by the BET and BJH methods [32], respectively. As can be seen from Table 1, the BET surface area of the LaMnO₃ sample is 14.275 m²/g. With the homogeneous introduction of CeO₂ into LaMnO₃, the BET surface area slightly decreases to 12.775 m²/g. The large specific surface area, in most cases, affords abundant active sites for gas absorption and serves as an important reason for the improvement of catalytic activity [33], but in this work, it is not a decisive factor, since the results of specific surface area are inconsistent with photo-thermal catalytic activities. Moreover, the toluene-TPD experiment result in Fig. S5 shows that CeO₂/LaMnO₃ hybrid exhibits stronger adsorption capability toward reactant than monocomponent CeO₂ and LaMnO₃, stemming from an intense interaction of LaMnO₃ with CeO₂.

To investigate the relative reducibility of CeO₂/LaMnO₃, H₂-TPR experiment was performed using LaMnO₃ and CeO₂ as reference samples. The normalized H₂-TPR profiles are shown in Fig. 6(a), and H₂ consumption calculated through quantitative integration of the corresponding TPR peak is listed in Table 1. The LaMnO₃ spectrum exhibits two obvious reduction peaks where the low temperature sharp peak in the range of 235–595 °C corresponds to the removal of a small amount of adsorbed oxygen species, reduction of Mn⁴⁺ to Mn³⁺ as well as a single electron reduction of Mn³⁺ located in a highly coordination-unsaturated microenvironment to Mn²⁺ [34,35]; whereas the high temperature broad peak centered at 829 °C, is most likely referred to the reduction of the remaining Mn³⁺ to Mn²⁺, leading to the collapse of perovskite phase and the formation of discrete oxide phases (La₂O₃ and MnO) [34]. The CeO₂ spectrum shows one small sharp peak centered at 514 °C and one broad peak at 812 °C, belonging to the reduction of surface-capping oxygen in lattice and the reduction of bulk oxygen of CeO₂ [36], respectively. The CeO₂/LaMnO₃ spectrum displays a broad peak centered at 343 °C with two shoulders and a large peak centered at 832 °C, respectively. It is noted that the center position of first reduction peak largely shifts to low temperature and its homologous H₂-uptake is significantly increased to 1296.0 μmol/g compared with those of pure CeO₂ with 60.9 μmol/g and LaMnO₃ with 410.5 μmol/g. Quantitative results of H₂-TPR for the overall temperature domain (50–910 °C) reveal that LaMnO₃ sample has greater H₂-uptake with a total of 3419.2 μmol/g than that of CeO₂/LaMnO₃ with 3373.9 μmol/g and CeO₂ with 920.8 μmol/g. However, in general, not all the oxygen atoms participate in the redox reaction, and reactive oxygen species such as surface lattice oxygen is closely related to catalytic performance which is reflected by low temperature reducibility, thus the initial H₂ consumption rate at low temperature is further

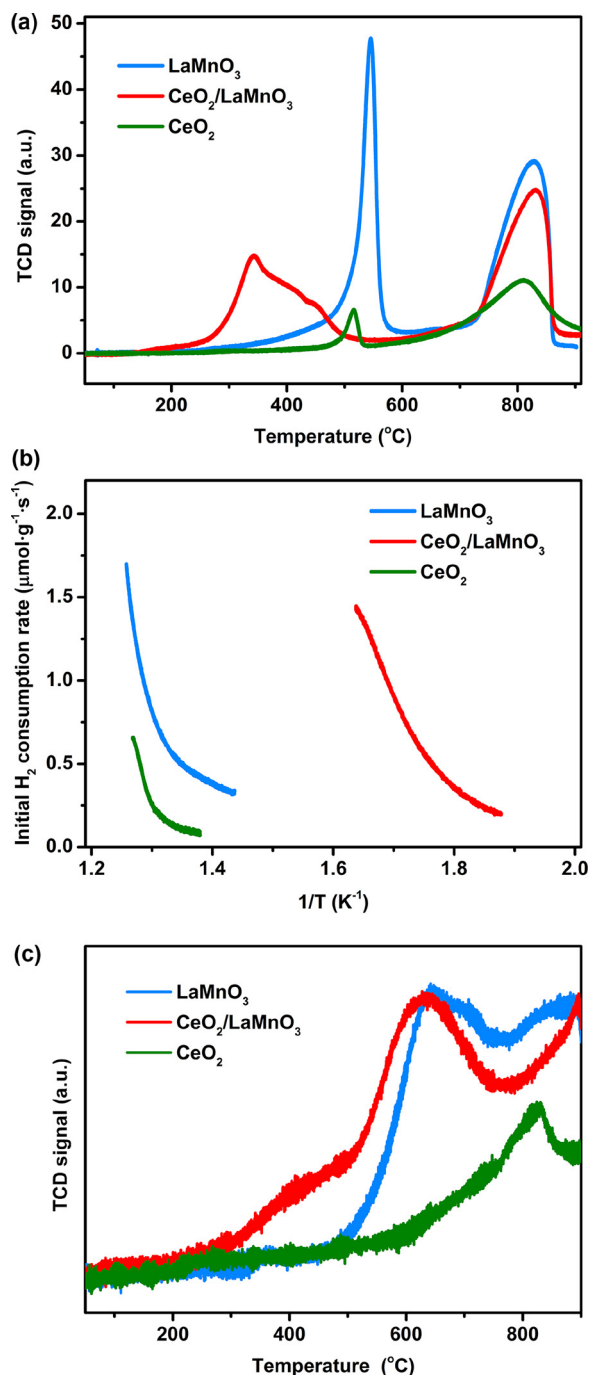


Fig. 6. (a) H₂-TPR profiles, (b) initial H₂ consumption rate at low temperature and (c) O₂-TPD at the temperature range of 50–900 °C.

applied to investigate the difference of reducibility [37]. As shown in Fig. 6(b), the low temperature H₂ consumption rates of the samples increase in the order of CeO₂ < LaMnO₃ < CeO₂/LaMnO₃, which implies that homogeneous introduction of CeO₂ into LaMnO₃ can enhance the low temperature reducibility of catalyst at operating temperature range.

The oxide with good reducibility generally presents abundant active oxygen species and this process proceeds at relatively low temperature or high oxygen mobility, allowing the transport of oxygen species with high efficiency [38]. O₂-TPD can be performed to investigate the type and mobility of oxygen species. Before the desorbed gas entered into the TCD, a cold trap was installed to avoid the effect of H₂O [39], and all the normalized results are shown in Fig. 6(c). For pure LaMnO₃

sample, no obvious oxygen desorption can be observed before 500 °C. As the temperature increased, a distinct desorption peak located at 642 °C with a shoulder at 711 °C as well as a wide range of peak centered at around 884 °C appear. For pure CeO₂ sample, the desorption oxygen initially occurs at 580 °C but proceeds slowly with increasing temperature. Obviously, a very intense peak appears at 826 °C with an overlapping shoulder around 735 °C. For the CeO₂/LaMnO₃ catalyst, three oxygen desorption regions in the temperature range of 280–500 °C, 500–780 °C and 780–900 °C are clearly observed. On the basis of literature results [37,40,41], the oxygen desorption peaks located temperature ranges at low temperature (100–200 °C) for desorption of adsorbed molecule oxygen or surface adsorbed peroxy species, at middle temperature (200–500 °C) for desorption of labile lattice oxygen on/near the surface layer of material and at high temperature (500–900 °C) for desorption of lattice oxygen from the framework of catalyst in the bulk, respectively. Many catalytic reactions, even under practical conditions, take place at the temperature less than 500 °C. Consequently, the main attention is focused on the oxygen desorption behavior of low/middle temperature. Moreover, the onset desorbed temperature of lattice oxygen species reflects the oxygen mobility. Compared with pure LaMnO₃ and CeO₂, the desorption area at the middle temperature of 200–500 °C was extremely enlarged with the formation of CeO₂/LaMnO₃ composite and the quantified results are listed in Table 1. The amount of desorbed surface lattice oxygen from the applied catalysts follows the sequence of CeO₂/LaMnO₃ > LaMnO₃ ≈ CeO₂. Thus, we can draw a conclusion that the homogeneous introduction of Ce into LaMnO₃ to form CeO₂/LaMnO₃ composite is beneficial to activate the surface lattice oxygen, accelerate oxygen transfer and enlarge its quantity [42].

XPS was further employed to investigate surface elemental compositions, chemical state and the nature of the adsorbed oxygen species in oxide samples. As shown in Fig. 7(a), an asymmetrical Mn 2p_{3/2} peak could be deconvoluted into two components with a binding energy of 641.6 and 643.3 eV, attributable to Mn³⁺ ions and Mn⁴⁺ ions, respectively, which indicates that Mn³⁺ and Mn⁴⁺ ions coexisted in LaMnO₃-based samples. The Ce 3d spectrum was composed of two multiplets (v and u), corresponding to the spin-orbit split 3d_{3/2} and 3d_{5/2} core holes. As shown in Fig. 7(b), the spin-orbit component is dominated by three features at Ce 3d⁹4f² O 2p⁴ (v ≈ 882.5 eV, u ≈ 900.6 eV), Ce 3d⁹4f¹ O 2p⁵ (v₂ ≈ 888.4 eV, u₂ ≈ 906.5 eV) and Ce 3d⁹4f⁰ O 2p⁶ (v₃ ≈ 897.9 eV, u₄ ≈ 916.0 eV) states, all referring to Ce⁴⁺ with different electron configuration states [43], which reveals that Ce⁴⁺ was the dominant species in the CeO₂/LaMnO₃ sample originating from the good stability of Ce⁴⁺ at high calcination temperature. As seen in Fig. 7(c), the asymmetrical O 1s spectrum of CeO₂/LaMnO₃ sample could be deconvoluted into three components with a binding energy of 529.3, 531.0, and 532.5 eV, corresponding to the surface lattice oxygen (O_{latt}), adsorbed oxygen (O_{ads}, e.g. O₂²⁻, O₂²⁻ or O⁻) and adsorbed molecular water [44,45], respectively. From the calculated O_{latt}/O_{ads} molar ratio in Table 1, the O_{latt} concentration of CeO₂/LaMnO₃ composite is much higher than that of LaMnO₃, but the surface Mn⁴⁺/Mn³⁺ molar ratios slightly decreased to 0.472. In addition, the O_{latt} species concentration is closely associated with the adsorption and/or activation of VOCs molecules, which suggests that a higher O_{latt} species concentration would be beneficial to the Mars-van Krevelen (MvK) oxidation reaction. In order to verify the nature of lattice oxygen involved in the oxidation of VOC over CeO₂/LaMnO₃, temperature-programmed surface reactions (TPSR) [46] were performed on a Quantachrome Chemstar automatic catalyst characterization system. 200 mg of each sample was loaded into a U-shape quartz reactor and purged with He at 300 °C for 1 h to remove adsorbed hydrates. Then, after cooling to room temperature the flowing gas was switched to a toluene/He for 1 h. Next, after saturation adsorption of toluene, the system was flushed with helium for 1 h and the catalyst was heated to 800 °C at a ramping rate of 10 °C min⁻¹. The reaction product generated during the TPSR experiment was monitored *in situ* by mass

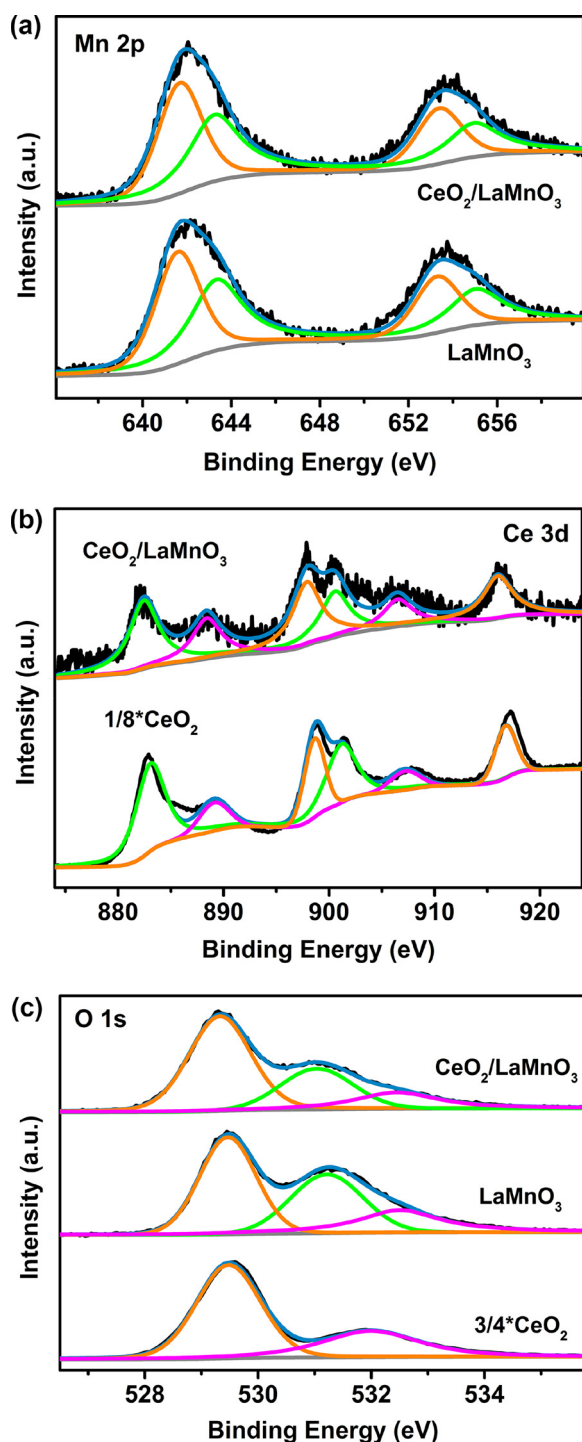


Fig. 7. (a) Mn 2p, (b) Ce 3d and (c) O 1s XPS spectra of CeO₂/LaMnO₃ composite (pure LaMnO₃ and CeO₂ are used for comparison).

spectroscopy, where the signal for mass-to-charge ratio $m/z = 44$ represents CO₂, $m/z = 18$ represents H₂O, $m/z = 32$ represents O₂ and $m/z = 92$ represents toluene. Under oxygen free atmosphere, both normalized $m/z = 44$ and $m/z = 18$ were detected during the TPSR for CeO₂/LaMnO₃ as shown in Fig. 8(a). The release of CO₂ (two oxygens from the oxide lattice) requires the extraction of lattice oxygen from metal oxides and the formation of oxygen vacancies during the TPSR, indicating the involvement of lattice oxygen in toluene oxidation (MVK mechanism). Of significance, lattice oxygen oxidation during the TPSR measured from CeO₂/LaMnO₃ is more pronounced than that for CeO₂ and LaMnO₃, as the normalized $m/z = 44$ signal in Fig. 8(b) detected

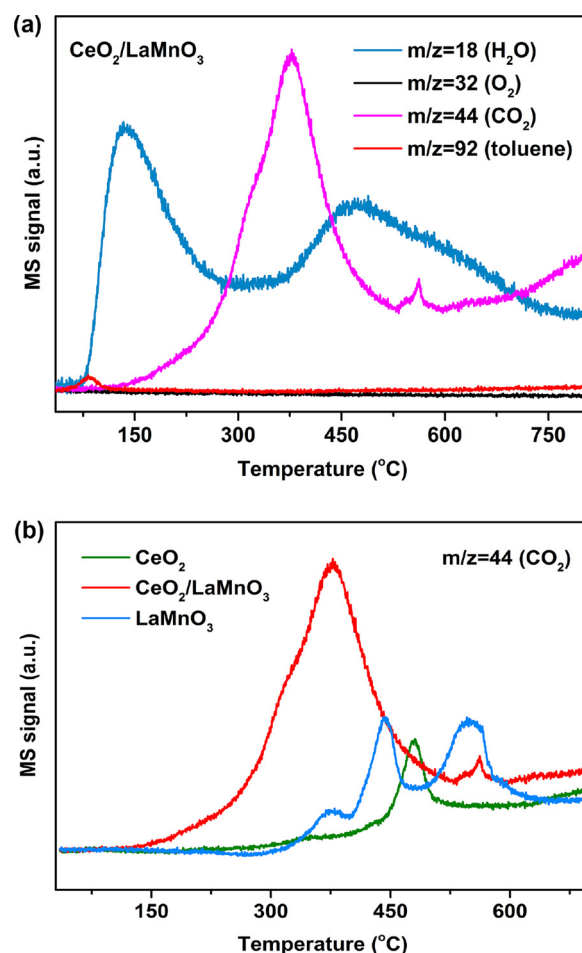


Fig. 8. MS signals collected at the exit of the reaction cell as a function of temperature over (a) CeO₂/LaMnO₃ during the TPSR experiment and (b) the comparison of CO₂ signal over CeO₂, LaMnO₃ and CeO₂/LaMnO₃ catalysts.

from CeO₂/LaMnO₃ composite is greater, implying a higher concentration of lattice oxygen species.

Why does CeO₂/LaMnO₃ composite achieve efficient photo-thermal catalytic activity? It has been widely accepted that catalytic oxidation of volatile organic compounds over reducible metal oxides follows a MVK mechanism where organic compounds react with surface lattice oxygen of metal oxides and leave behind oxygen vacancies on the surface which are subsequently replenished by dissociated molecular oxygen [47]. The key characteristic feature of MVK mechanism is that the oxide surface is directly involved via its most reactive surface lattice oxygen atoms, rather than just a spectator of the reaction. To validate whether or not MVK mechanism also occurs on CeO₂/LaMnO₃ composite, *in situ* DRIFTS spectroscopy was performed to inspect the effect of surface lattice oxygen on toluene oxidation reactivity [48]. Prior to toluene adsorption and reaction experiments, the catalyst was flushed with high-purity N₂ at 260 °C for 1 h to remove adsorbed impurities (background spectrum was collected and automatically deducted from the sample spectra), and afterwards 1000 ppm toluene/N₂ was introduced to the cell at a flow rate of 50 mL/min at 260 °C a series of DRIFTS spectra recorded during gaseous toluene/N₂ exposure over CeO₂/LaMnO₃ catalyst are displayed in Fig. 9. The broad peaks at 2962, 2918, 2868 and 2848 cm⁻¹ are associated with C–H stretching vibrations of the aromatic ring and asymmetric/symmetric C–H stretching vibrations of methyl group [49]. The weak band at 1234 cm⁻¹ is characteristic of ring vibrations [27]. These absorption peaks develop rapidly and reach steady level within a few minutes after the introduction of gaseous toluene into the cell. In particular, an intense

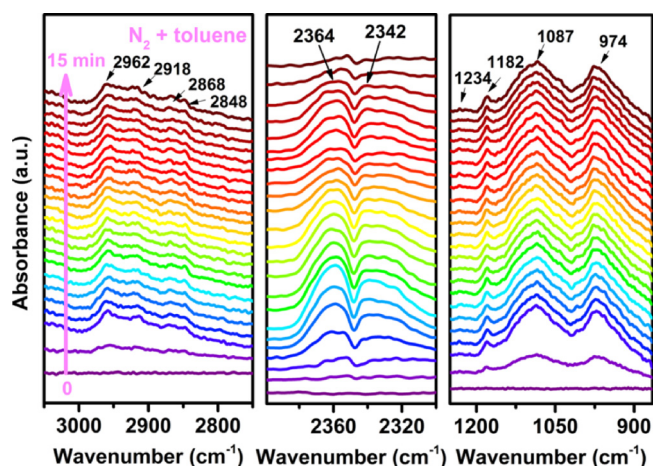


Fig. 9. *In situ* DRIFTS spectra of adsorbed species on $\text{CeO}_2/\text{LaMnO}_3$ catalyst in a toluene/ N_2 feed gas upon heating at 260°C .

peak at 1182 cm^{-1} with a small shoulder at 1087 cm^{-1} can be assigned to C–O stretching vibration of an alkoxide species [50]. The peak at 974 cm^{-1} corresponds to the bending vibration and torsional vibration of CH_2 [51]. The appearance of these absorption peaks indicate that the C–H bond of methyl group of aromatic ring is cleaved to generate C–O bond in which the oxygen atoms come from the catalyst, giving rise to a benzoyl intermediate ($\text{C}_6\text{H}_5\text{--CH}_2\text{--O}$) [39], which is attached to the surface of $\text{CeO}_2/\text{LaMnO}_3$. The new doublet peaks located at 2364 and 2342 cm^{-1} are characteristic of asymmetric $\text{O}=\text{C}=\text{O}$ stretching vibrations [52,53], and the intensities of their peaks linearly increase with time on stream then decrease to zero, due to the contribution of generated CO_2 from deep oxidation of adsorbed toluene species with the limited supply of lattice oxygen. Because the involvement of adsorbed oxygen or gaseous oxygen in the activation of toluene is entirely excluded, these observations support the assumption that this oxidation reaction on $\text{CeO}_2/\text{LaMnO}_3$ catalyst follows a MvK mechanism where adsorbed toluene can actively react with surface lattice oxygen to give final product CO_2 under oxygen-free condition.

The oxidation of toluene occurs by means of the surface lattice oxygen of the catalyst, thus, refilling of oxygen vacancies is of great importance for the oxidation process. To reveal more details of the reaction on catalyst surface and identify the evolved surface chemical species, *in situ* DRIFTS was also performed in a flow of toluene/ $21\%\text{ O}_2/\text{N}_2$ feed gas. In Fig. 10, each spectrum was collected during 30 min oxidation reaction at the specified temperature. In contrast to oxygen-free feed experiment, CO_2 doublet peaks around 2364 and 2342 cm^{-1} are also clearly observed at the temperature of 100°C or above and the intensities of CO_2 peaks are gradually intensified with the elevated temperature. Notably, the new peaks at 3080 , 3042 and 3033 cm^{-1} are associated with C–H stretching vibrations of aromatic ring of an undissociated adsorbed toluene molecule, which is accompanied by the peaks at 2937 and 2884 cm^{-1} representing asymmetric and symmetric C–H stretching vibrations of methyl group, and by the peaks at 1602 and 1500 cm^{-1} representing in-plane skeletal vibration of the aromatic ring. Even after elevating the sample temperature to 260°C , the IR features of all three types of adsorbed toluene remain very stable. The weak peaks at 1085 and 1032 cm^{-1} are associated with C–O stretching vibration of adsorption intermediates of toluene [50,54]. Note that the peak assigned to CH_2 at around 970 cm^{-1} is not observed in a toluene/ $20\%\text{ O}_2$ feed gas, suggesting that the H of CH_3 group is not abstracted. These observations clearly demonstrate that gaseous toluene molecule adsorbed onto the surface of $\text{CeO}_2/\text{LaMnO}_3$ through a weak interaction of the aromatic ring with the catalyst [39], rather than through benzoyl oxide species ($\text{C}_6\text{H}_5\text{--CH}_2\text{--O}$). In order to track the intermediates during the adsorption/oxidation process of toluene, *in situ* DRIFTS is

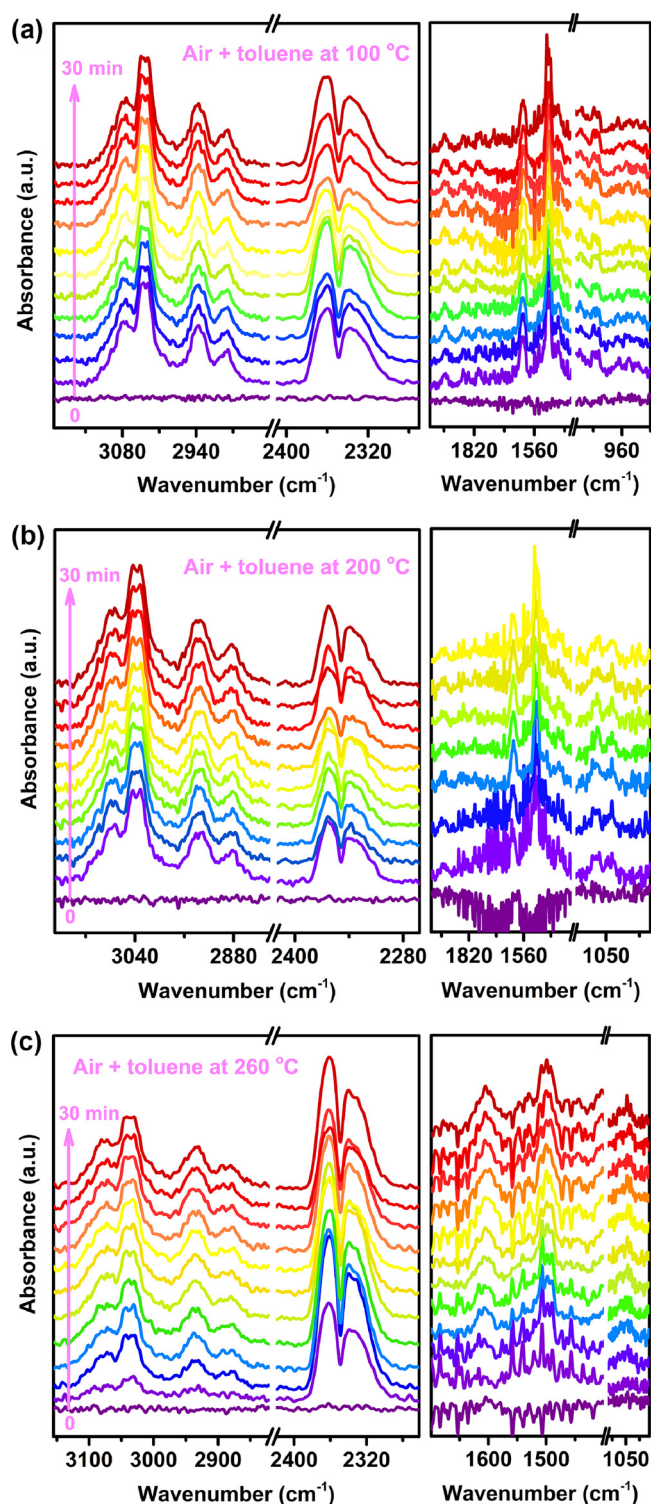


Fig. 10. *In situ* DRIFTS spectra of adsorbed species on $\text{CeO}_2/\text{LaMnO}_3$ composite in a toluene/ $21\%\text{ O}_2/\text{N}_2$ feed gas upon heating at the temperature of (a) 100°C , (b) 200°C and (c) 260°C .

applied again to investigate its partial oxidation at low temperature. A pure air gas bubbling through a liquid toluene was introduced to the $\text{CeO}_2/\text{LaMnO}_3$ composite for 60 min. Subsequently, only pure air gas was introduced to investigate the intermediates at ambient temperature or above. The recorded spectra are shown in Fig. 11(a). The peaks at 1608 , 1450 and 1381 cm^{-1} are observable at the temperature of 35°C , and can be assigned to C=O vibration of benzoquinone derivative

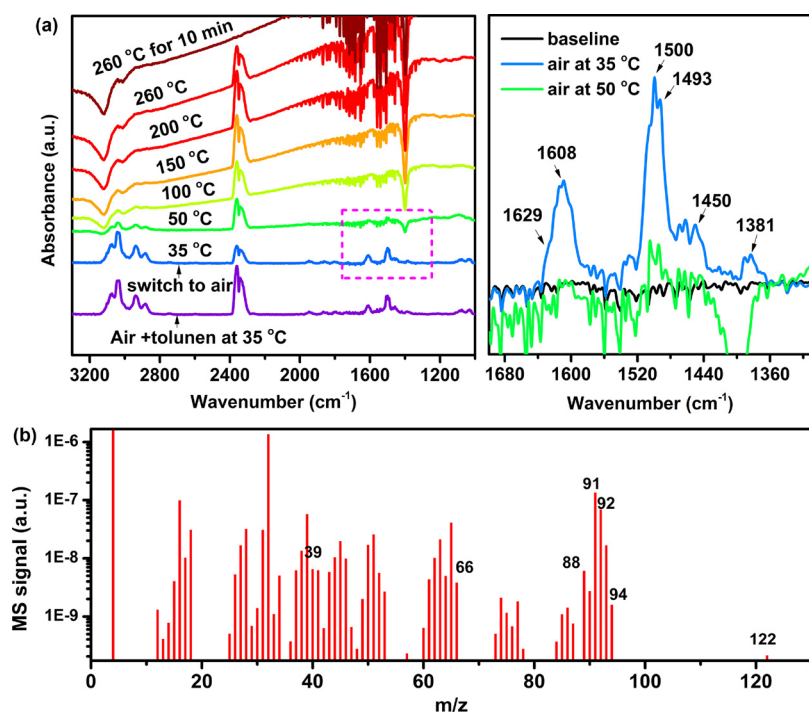


Fig. 11. (a) *In situ* DRIFTS spectra of adsorbed species on CeO₂/LaMnO₃ composite after a continuous toluene/air feed gas at ambient temperature and then replaced by pure air gas upon heating at the elevated temperature, and the right image of (a) is the enlarged area marked by the pink box; (b) On-line MS spectrum for catalytic oxidation of toluene over CeO₂/LaMnO₃ at the reaction temperature of 260 °C in a flow of toluene/21% O₂/N₂ feed gas, and the organic components in outlet gas containing toluene ($m/e = 92, 91, 65, 63, 39$) and benzoquinone derivative ($m/z = 122, 94, 88, 66, 39$).

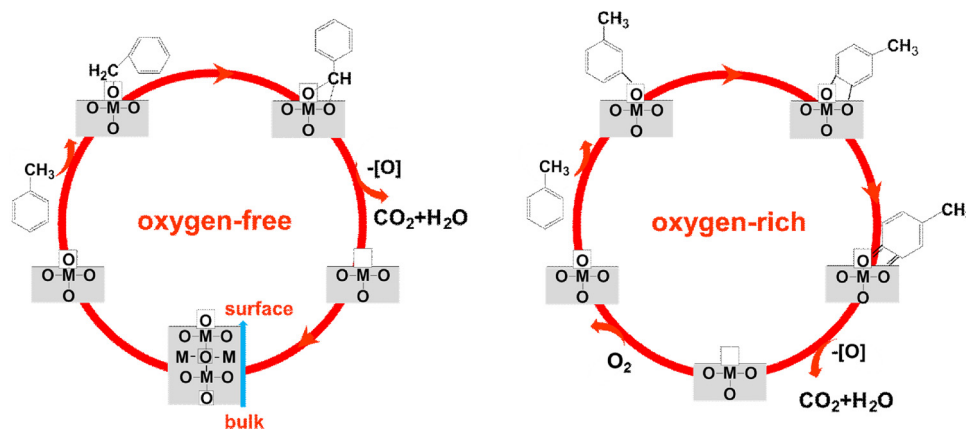


Fig. 12. The plausible reaction mechanism for toluene oxidation over CeO₂/LaMnO₃ catalyst with and without oxygen atmosphere.

[55–57]. A TPO experiment further performed to verify the formation of benzoquinone derivative such as 4-methyl-1,2-benzoquinone on basis of characteristic fraction peaks ($m/z = 122, 94, 88, 66, 39$) recorded by on-line MS as shown in Fig. 11(b). Based on the above DRIFTS and TPO observations, a plausible reaction mechanism for toluene oxidation over CeO₂/LaMnO₃ catalyst is proposed and shown in Fig. 12. Upon IR irradiation, photo-thermal responsive CeO₂/LaMnO₃ composite achieves broad spectrum utilization for thermalization where black CeO₂/LaMnO₃ via hole polarons within localized charge transfer vibronic excitons absorbs IR light, releases the absorbed light energy in the form of heat and ultimately dissipates into the surrounding medium. When the local temperature increases above the light-off temperature of toluene thermocatalytic reaction on CeO₂/LaMnO₃ composite, the thermocatalytic reaction occurs via a MvK mechanism. Under oxygen-rich condition, the toluene molecule is firstly adsorbed on the surface oxygen lattice of CeO₂/LaMnO₃ catalyst via the three possible sites (ortho-, meta-, or para-). Then, hydrogen atoms are abstracted from the aromatic ring of toluene by surface oxygen lattice to produce benzoquinone derivative [55,57]. These intermediates are further oxidized by surface lattice oxygen atoms located at low-coordinated sites on the CeO₂/LaMnO₃ and completely

decomposed to final products of CO₂ and H₂O, simultaneously leaving behind oxygen vacancies on the surface where metal oxide lose oxygen atoms and donate them to the adsorbed toluene molecule during the process. Subsequently, molecular oxygen can adsorb onto the surface of CeO₂/LaMnO₃ composite, dissociate and eventually refill vacancies created in the oxidative process [58], by which the continuous efficient catalytic oxidation of toluene proceeds. Consequently, the rate of oxidation/reduction cycle and oxygen desorption capacity of a catalyst play very significant roles in catalytic oxidation reactions [59]. In this work, the catalytic performance of material increases with elevating low temperature reducibility and accelerating lattice oxygen mobility, which accounts for the enhancement activity of CeO₂/LaMnO₃.

4. Conclusion

The utilization of renewable solar energy via infrared light photo-thermocatalysis provides a potential alternative strategy in environmental pollutants purification. Noble metal free CeO₂/LaMnO₃ hybrid exhibits ultrabroadband strong light absorption, efficient light-to-heat conversion, good low temperature reducibility and high lattice oxygen mobility, giving a prominent toluene conversion of 89% and CO₂ yield

of 87% under IR irradiation intensity of 280 mW/cm², together with excellent stability. This work highlights that LaMnO₃-based composite as IR light photon absorber shows great promise for redox reactions through photo-thermal effect, which provides an alternative and feasible strategy for solar energy conversion.

Acknowledgments

This work was supported by the Natural Science Foundation of Fujian Province of China [Nos. 2016J01079, 2016J05049]; One Hundred Talent Project and the Key Program for Frontier Sciences-Youth Scientist from Chinese Academy of Sciences [QYZDB-SSW-DQC022]; National Natural Science Foundation of China [Nos. 21501175, 21703233]; Key Project of National Natural Science Foundation of China [U1463204]; Natural Science Foundation (NSF) of Fujian Province for Distinguished Young Investigator Rolling Grant [2017J07002].

Appendix A. Supplementary data

Supplementary material related to this article can be found, in the online version, at doi:<https://doi.org/10.1016/j.apcatb.2018.08.069>.

References

- A.H. Goldstein, I.E. Galbally, Known and unexplored organic constituents in the earth's atmosphere, *Environ. Sci. Technol.* 41 (2007) 1514–1521.
- C. George, M. Ammann, B. D'Anna, D.J. Donaldson, S.A. Nizkorodov, Heterogeneous photochemistry in the atmosphere, *Chem. Rev.* 115 (2015) 4218–4258.
- S. Royer, D. Duprez, F. Can, X. Courtois, C. Batiot-Dupeyrat, S. Laassiri, H. Alamdari, Perovskites as substitutes of noble metals for heterogeneous catalysis: dream or reality, *Chem. Rev.* 114 (2014) 10292–10368.
- H.Y. Zhu, P.F. Zhang, S. Dai, Recent advances of lanthanum-based perovskite oxides for catalysis, *ACS Catal.* 5 (2015) 6370–6385.
- B. Levasseur, S. Kaliaguine, Methanol oxidation on LaBO₃ (B = Co, Mn, Fe) perovskite-type catalysts prepared by reactive grinding, *Appl. Catal. A-Gen.* 343 (2008) 29–38.
- M.C. Alvarez-Galvan, V.A.D. O'Shea, G. Arzamendi, B. Pawelec, L.M. Gandia, J.L.G. Fierro, Methyl ethyl ketone combustion over La-transition metal (Cr, Co, Ni, Mn) perovskites, *Appl. Catal. B-Environ.* 92 (2009) 445–453.
- C.H. Zhang, C. Wang, S. Gil, A. Boreave, L. Retailleau, Y.L. Guo, J.L. Valverde, A. Giroir-Fendler, Catalytic oxidation of 1,2-dichloropropane over supported LaMnO_x oxides catalysts, *Appl. Catal. B-Environ.* 201 (2017) 552–560.
- N. Armaroli, V. Balzani, The future of energy supply: challenges and opportunities, *Angew. Chem. Int. Ed.* 46 (2007) 52–66.
- Y.H. Ng, S. Ikeda, M. Matsumura, R. Amal, A perspective on fabricating carbon-based nanomaterials by photocatalysis and their applications, *Energy Environ. Sci.* 5 (2012) 9307–9318.
- L.X. Zhong, J.J. Branch, S. Batterman, B.M. Bartlett, C. Godwin, Experimental and modeling study of visible light responsive photocatalytic oxidation (PCO) materials for toluene degradation, *Appl. Catal. B-Environ.* 216 (2017) 122–132.
- B.Y. Xu, Y. An, Y.Y. Liu, X.Y. Qin, X.Y. Zhang, Y. Dai, Z.Y. Wang, P. Wang, M.H. Whangbo, B.B. Huang, Enhancing the photocatalytic activity of BiOX (X = Cl, Br, and I), BiO₂CO₃ and Bi₂O₃ by modifying their surfaces with polar organic anions, 4-substituted thiophenolates, *J. Mater. Chem. A* 5 (2017) 14406–14414.
- D.M. Schultz, T.P. Yoon, Solar synthesis: prospects in visible light photocatalysis, *Science* 343 (2014) 1239176–1239110.
- J.-J. Li, S.-C. Cai, E.-Q. Yu, B. Weng, H.-P. Jia, Y.-J. Xu, Efficient infrared light promoted degradation of volatile organic compounds over photo-thermal responsive Pt-rGO-TiO₂ composites, *Appl. Catal. B-Environ.* 233 (2018) 260–271.
- V.S. Vikhnin, S. Kapphan, B.A. Melekh, E.B. Shadrin, Jahn-Teller polarons and peculiarities of their absorption in LaMnO₃ and La_{1-x}Sr_xMnO₃ perovskite-like systems, *Ferroelectrics* 235 (1999) 211–220.
- M. Wierschem, S. Kapphan, V.S. Vikhnin, IR absorption of trapped and free Jahn-Teller polarons in 3D-crystals and films of LaMnO₃ and La_{2/3}Sr_{1/3}MnO₃, *Ferroelectrics* 299 (2004) 49–54.
- N.N. Loshkareva, Y.P. Sukhorukov, E.V. Mostovshchikova, L.V. Nomerovannaya, A.A. Makhnev, S.V. Naumov, E.A. Gan'shina, I.K. Rodin, A.S. Moskvina, A.M. Balbashov, The evolution of the optical spectra of LaMnO₃ under light n- and p-type doping and the separation of phases, *J. Exp. Theor. Phys.* 94 (2002) 350–355.
- J. Chen, Z. He, G. Li, T. An, H. Shi, Y. Li, Visible-light-enhanced photo-thermocatalytic activity of ABO₃-type perovskites for the decontamination of gaseous styrene, *Appl. Catal. B-Environ.* 209 (2017) 146–154.
- P. Zhang, Y. Liu, B.Z. Tian, Y.S. Luo, J.L. Zhang, Synthesis of core-shell structured CdS@CeO₂ and CdS@TiO₂ composites and comparison of their photocatalytic activities for the selective oxidation of benzyl alcohol to benzaldehyde, *Catal. Today* 281 (2017) 181–188.
- S. Singh, S.L. Lo, Single-phase cerium oxide nanospheres: an efficient photocatalyst for the abatement of rhodamine B dye, *Environ. Sci. Pollut. R.* 25 (2018) 6532–6544.
- Y.H. Zhang, Z.R. Tang, X.Z. Fu, Y.J. Xu, TiO₂-graphene nanocomposites for gas-phase photocatalytic degradation of volatile aromatic pollutant: is TiO₂-graphene truly different from other TiO₂-carbon composite materials? *ACS Nano* 4 (2010) 7303–7314.
- H. Li, X.L. Cui, A hydrothermal route for constructing reduced graphene oxide/TiO₂ nanocomposites: enhanced photocatalytic activity for hydrogen evolution, *Int. J. Hydrogen Energy* 39 (2014) 19877–19886.
- J.F. Huang, C.X. Liu, Y.H. Zhu, S. Masala, E. Alarousi, Y. Han, A. Fratalocchi, Harnessing structural darkness in the visible and infrared wavelengths for a new source of light, *Nat. Nanotechnol.* 11 (2016) 60–67.
- D.Q. Gong, H.D. Liu, G. Luo, P. Zhang, X.D. Cheng, B. Yang, Y.B. Wang, J. Min, W.X. Wang, S.P. Chen, Z.Q. Cui, K.W. Li, L.F. Hu, Thermal aging test of AlCrNO-based solar selective absorbing coatings prepared by cathodic arc plating, *Sol. Energy Mater. Sol. Cells* 136 (2015) 167–171.
- M. Gao, P.K.N. Connor, G.W. Ho, Plasmonic photothermal directed broadband sunlight harnessing for seawater catalysis and desalination, *Energy Environ. Sci.* 9 (2016) 3151–3160.
- X. Chen, X. Chen, S.C. Cai, J. Chen, W.J. Xu, H.P. Jia, J. Chen, Catalytic combustion of toluene over mesoporous Cr₂O₃-supported platinum catalysts prepared by in situ pyrolysis of MOFs, *Chem. Eng. J.* 334 (2018) 768–779.
- J. Chen, X. Chen, W.J. Xu, Z. Xu, J.Z. Chen, H.P. Jia, J. Chen, Hydrolysis driving redox reaction to synthesize Mn-Fe binary oxides as highly active catalysts for the removal of toluene, *Chem. Eng. J.* 330 (2017) 281–293.
- X.Y. Wang, Y. Liu, T.H. Zhang, Y.J. Luo, Z.X. Lan, K. Zhang, J.C. Zuo, L.L. Jiang, R.H. Wang, Geometrical-site-dependent catalytic activity of ordered mesoporous Co-based spinel for benzene oxidation: *in situ* DRIFTS study coupled with raman and XAFS spectroscopy, *ACS Catal.* 7 (2017) 1626–1636.
- Y.Z. Li, J.C. Huang, T. Peng, J. Xu, X.J. Zhao, Photocatalytic synergetic effect leads to high efficient detoxification of benzene on TiO₂ and Pt/TiO₂ nanocomposite, *ChemCatChem* 2 (2010) 1082–1087.
- Z. Wang, Z. Quan, J. Lin, Remarkable changes in the optical properties of CeO₂ nanocrystals induced by lanthanide ions doping, *Inorg. Chem.* 46 (2007) 5237–5242.
- J.T. Hou, Y.Z. Li, M.Y. Mao, Y.Z. Yue, G.N. Greaves, X.J. Zhao, Full solar spectrum light driven thermocatalysis with extremely high efficiency on nanostructured Ce ion substituted OMS-2 catalyst for VOCs purification, *Nanoscale* 7 (2015) 2633–2640.
- M.Y. Mao, Y.Z. Li, J.T. Hou, M. Zeng, X.J. Zhao, Extremely efficient full solar spectrum light driven thermocatalytic activity for the oxidation of VOCs on OMS-2 nanorod catalyst, *Appl. Catal. B-Environ.* 174 (2015) 496–503.
- D. Trong On, S. Kaliaguine, Ultrastable and highly acidic, zeolite-coated mesoporous aluminosilicates, *Angew. Chem. Int. Ed.* 41 (2002) 1036–1040.
- L. Huang, X. Hu, S. Yuan, H. Li, T. Yan, L. Shi, D. Zhang, Photocatalytic preparation of nanostructured MnO₂-Co₃O₄/TiO₂ hybrids: the formation mechanism and catalytic application in SCR deNO_x reaction, *Appl. Catal. B-Environ.* 203 (2017) 778–788.
- F. Teng, W. Han, S. Liang, B. Gaugeu, R. Zong, Y. Zhu, Catalytic behavior of hydrothermally synthesized La_{0.5}Sr_{0.5}MnO₃ single-crystal cubes in the oxidation of CO and CH₄, *J. Catal.* 250 (2007) 1–11.
- Y. Liu, H. Dai, J. Deng, Y. Du, X. Li, Z. Zhao, Y. Wang, B. Gao, H. Yang, G. Guo, *In situ* poly(methyl methacrylate)-templating generation and excellent catalytic performance of MnO_x/3DOM LaMnO₃ for the combustion of toluene and methanol, *Appl. Catal. B-Environ.* 140 (2013) 493–505.
- H.Q. Zhu, Z.F. Qin, W.J. Shan, W.J. Shen, J.G. Wang, Pd/CeO₂-TiO₂ catalyst for CO oxidation at low temperature: a TPR study with H₂ and CO as reducing agents, *J. Catal.* 225 (2004) 267–277.
- J. Chen, X. Chen, X. Chen, W. Xu, Z. Xu, H. Jia, J. Chen, Homogeneous introduction of CeO₂ into MnO_x-based catalyst for oxidation of aromatic VOCs, *Appl. Catal. B-Environ.* 224 (2018) 825–835.
- S.P. Mo, S.D. Li, J.Q. Li, Y.Z. Deng, S.P. Peng, J.Y. Chen, Y.F. Chen, Rich surface Co (III) ions-enhanced Co nanocatalyst benzene/toluene oxidation performance derived from Co^{II}/Co^{III} layered double hydroxide, *Nanoscale* 8 (2016) 15763–15773.
- H. Sun, Z.G. Liu, S. Chen, X. Quan, The role of lattice oxygen on the activity and selectivity of the OMS-2 catalyst for the total oxidation of toluene, *Chem. Eng. J.* 270 (2015) 58–65.
- Y. Zheng, W. Wang, D. Jiang, L. Zhang, X. Li, Z. Wang, Ultrathin mesoporous Co₃O₄ nanosheets with excellent photo-/thermo-catalytic activity, *J. Mater. Chem. A* 4 (2016) 105–112.
- L. Yu, G. Diao, F. Ye, M. Sun, J. Zhou, Y. Li, Y. Liu, Promoting effect of Ce in Ce/OMS-2 catalyst for catalytic combustion of dimethyl ether, *Catal. Lett.* 141 (2011) 111–119.
- C. Liu, H. Xian, Z. Jiang, L. Wang, J. Zhang, L. Zheng, Y. Tan, X. Li, Insight into the improvement effect of the Ce doping into the SnO₂ catalyst for the catalytic combustion of methane, *Appl. Catal. B-Environ.* 176 (2015) 542–552.
- M. Zhang, M.A. Farid, Y. Wang, J.L. Xie, J.L. Geng, H. Zhang, J.L. Sun, G.B. Li, F.H. Liao, J.H. Lin, Superconductivity in perovskite Ba_{1-x}Ln_xBi_{0.20}Pb_{0.80}O_{3-δ} (Ln = La, Ce, Pr, Nd, Sm, Eu, Gd, Tb, Dy, Ho, Er, Tm, Yb, Lu), *Inorg. Chem.* 57 (2018) 1269–1276.
- Y.X. Liu, H.X. Dai, J.G. Deng, S.H. Xie, H.G. Yang, W. Tan, W. Han, Y. Jiang, G.S. Guo, Mesoporous Co₃O₄-supported gold nanocatalysts: highly active for the oxidation of carbon monoxide, benzene, toluene, and o-xylene, *J. Catal.* 309 (2014) 408–418.

- [45] S.H. Xie, Y.X. Liu, J.G. Deng, X.T. Zhao, J. Yang, K.F. Zhang, Z. Han, H.X. Dai, Three-dimensionally ordered macroporous CeO₂-supported Pd@Co nanoparticles: highly active catalysts for methane oxidation, *J. Catal.* 342 (2016) 17–26.
- [46] V.P. Santos, M.F.R. Pereira, J.J.M. Orfao, J.L. Figueiredo, The role of lattice oxygen on the activity of manganese oxides towards the oxidation of volatile organic compounds, *Appl. Catal. B-Environ.* 99 (2010) 353–363.
- [47] A.R. Puigdollers, P. Schlexer, S. Tosoni, G. Pacchioni, Increasing oxide reducibility: the role of metal/oxide interfaces in the formation of oxygen vacancies, *ACS Catal.* 7 (2017) 6493–6513.
- [48] Y.G. Wang, D.C. Cantu, M.S. Lee, J. Li, V.A. Glezakou, R. Rousseau, CO oxidation on Au/TiO₂: condition-dependent active sites and mechanistic pathways, *J. Am. Chem. Soc.* 138 (2016) 10467–10476.
- [49] M.J. Wang, F. Zhang, X.D. Zhu, Z.M. Qi, B. Hong, J.J. Ding, J. Bao, S. Sun, C. Gao, DRIFTS evidence for facet-dependent adsorption of gaseous toluene on TiO₂ with relative photocatalytic properties, *Langmuir* 31 (2015) 1730–1736.
- [50] Z.R. Zhu, F.Y. Liu, W. Zhang, Fabricate and characterization of Ag/BaAl₂O₄ and its photocatalytic performance towards oxidation of gaseous toluene studied by FTIR spectroscopy, *Mater. Res. Bull.* 64 (2015) 68–75.
- [51] V. Augugliaro, H. Kisch, V. Loddo, M.J. Lopez-Munoz, C. Marquez-Alvarez, G. Palmisano, L. Palmisano, F. Parrino, S. Yurdakal, Photocatalytic oxidation of aromatic alcohols to aldehydes in aqueous suspension of home prepared titanium dioxide 2. Intrinsic and surface features of catalysts, *Appl. Catal. A-Gen.* 349 (2008) 189–197.
- [52] X. Wang, H. Shi, J.H. Kwak, J. Szanyi, Mechanism of CO₂ hydrogenation on Pd/Al₂O₃ catalysts: kinetics and transient DRIFTS-MS studies, *ACS Catal.* 5 (2015) 6337–6349.
- [53] W.C. Wilfong, C.S. Srikanth, S.S.C. Chuang, *In situ* ATR and DRIFTS studies of the nature of adsorbed CO₂ on tetraethylenepentamine films, *ACS Appl. Mater. Interfaces* 6 (2014) 13617–13626.
- [54] W. Rachmady, M.A. Vannice, Acetic acid reduction by H₂ over supported Pt catalysts: a DRIFTS and TPD/TPR study, *J. Catal.* 207 (2002) 317–330.
- [55] J. Lichtenberger, M.D. Amiridis, Catalytic oxidation of chlorinated benzenes over V₂O₅/TiO₂ catalysts, *J. Catal.* 223 (2004) 296–308.
- [56] K.Z. Li, J.J. Chen, B.Y. Bai, S. Zhao, F.Y. Hu, J.H. Li, Bridging the reaction route of toluene total oxidation and the structure of ordered mesoporous Co₃O₄: the roles of surface sodium and adsorbed oxygen, *Catal. Today* 297 (2017) 173–181.
- [57] J. Wang, X. Wang, X.L. Liu, T.Y. Zhu, Y.Y. Guo, H. Qi, Catalytic oxidation of chlorinated benzenes over V₂O₅/TiO₂ catalysts: the effects of chlorine substituents, *Catal. Today* 241 (2015) 92–99.
- [58] D. Widmann, R.J. Behm, Activation of molecular oxygen and the nature of the active oxygen species for CO oxidation on oxide supported Au catalysts, *Acc. Chem. Res.* 47 (2014) 740–749.
- [59] M. Machida, K. Eguchi, H. Arai, Effect of structural modification on the catalytic property of Mn-substituted hexaaluminates, *J. Catal.* 123 (1990) 477–485.